HHS Public Access

Author manuscript

Int J Radiat Oncol Biol Phys. Author manuscript; available in PMC 2017 May 31.

Published in final edited form as:

Int J Radiat Oncol Biol Phys. 2016 July 15; 95(4): 1281–1289. doi:10.1016/j.ijrobp.2016.03.002.

Image Guided Radiation Therapy Using Synthetic Computed Tomography Images in Brain Cancer

Ryan G. Price, BS[*,†], **Joshua P. Kim, PhD**[*], **Weili Zheng, PhD**[*], **Indrin J. Chetty, PhD**[*,†], and **Carri Glide-Hurst, PhD**[*,†]

[*]Department of Radiation Oncology, Henry Ford Health System, Detroit, Michigan

[†]Department of Radiation Oncology, Wayne State University School of Medicine, Detroit, Michigan

Abstract

Purpose—The development of synthetic computed tomography (CT) (synCT) derived from magnetic resonance (MR) images supports MR-only treatment planning. We evaluated the accuracy of synCT and synCT-generated digitally reconstructed radiographs (DRRs) relative to CT and determined their performance for image guided radiation therapy (IGRT).

Methods and Materials—Magnetic resonance simulation (MR-SIM) and CT simulation (CT-SIM) images were acquired of an anthropomorphic skull phantom and 12 patient brain cancer cases. SynCTs were generated using fluid attenuation inversion recovery, ultrashort echo time, and Dixon data sets through a voxel-based weighted summation of 5 tissue classifications. The DRRs were generated from the phantom synCT, and geometric fidelity was assessed relative to CT-generated DRRs through bounding box and landmark analysis. An offline retrospective analysis was conducted to register cone beam CTs (n=34) to synCTs and CTs using automated rigid registration in the treatment planning system. Planar MV and KV images (n=37) were rigidly registered to synCT and CT DRRs using an in-house script. Planar and volumetric registration reproducibility was assessed and margin differences were characterized by the van Herk formalism.

Results—Bounding box and landmark analysis of phantom synCT DRRs were within 1 mm of CT DRRs. Absolute planar registration shift differences ranged from 0.0 to 0.7 mm for phantom DRRs on all treatment platforms and from 0.0 to 0.4 mm for volumetric registrations. For patient planar registrations, the mean shift differences were 0.4 ± 0.5 mm (range, −0.6 to 1.6 mm), 0.0 ± 0.5 mm (range, −0.9 to 1.2 mm), and 0.1 ± 0.3 mm (range, −0.7 to 0.6 mm) for the superior-inferior (S-I), left-right (L-R), and anterior-posterior (A-P) axes, respectively. The mean shift differences in volumetric registrations were 0.6 ± 0.4 mm (range, −0.2 to 1.6 mm), 0.2 ± 0.4 mm (range, −0.3 to 1.2 mm), and 0.2 ± 0.3 mm (range, −0.2 to 1.2 mm) for the S-I, L-R, and A-P axes, respectively. The CT-SIM and synCT derived margins were <0.3 mm different.

Reprint requests to: Carri Glide-Hurst, PhD, Department of Radiation Oncology, Henry Ford Health System, 2799 West Grand Boulevard, Detroit, MI 48202. Tel: (313) 916-8447.; churst2@hfhs.org.

Conflict of interest: The submitting institution holds research agreements with Philips Healthcare. The authors report no other conflict of interest.

Supplementary material for this article can be found at www.redjournal.org.

Conclusion—DRRs generated by synCT were in close agreement with CT-SIM. Planar and volumetric image registrations to synCT-derived targets were comparable with CT for phantom and patients. This validation is the next step toward MR-only planning for the brain.

Introduction

The standard of care for brain radiation therapy (RT) is to use magnetic resonance imaging (MRI) to delineate the target and organs at risk followed by image registration to transfer these contours to the computed tomography (CT) image for treatment planning. However, it has been shown that systematic uncertainties ranging from 1 to 2 mm can be introduced from the MRI-to-CT coregistration process in the brain (1, 2). MR-only treatment planning has the potential to reduce these uncertainties while also decreasing the clinical workload. Unfortunately, it is limited by both patient-dependent and system-dependent geometric distortion (3, 4) and by the lack of electron density information provided by MRI intensity values.

We (5, 6) and others (7–12) have developed methods for generating synthetic or pseudo CTs to support MR-only treatment planning, including approaches such as Gaussian mixture modeling (GMM) (8), atlas-based solutions (10), and patch based using nearest-neighbor intensity values (9). The dosimetric differences resulting from the use of synthetic computed tomography images (synCTs) have been shown to be clinically negligible (<2% for planning target volume [PTV] metrics) (6, 9, 11, 13–15). However, further study implementing synCTs as the reference data sets for linac-based image guided radiation therapy (IGRT) will help determine their robustness in an MR-only workflow. Qualitative evaluation of digitally reconstructed radiographs (DRRs) derived from MRI data has shown promise (7). Our work builds on the current literature (12, 16, 17) by including quantitative comparisons of synCT and CT, benchmarking results in a novel MR-CT-compatible brain phantom, including both planar and volumetric evaluations, and using multiple IGRT platforms for analysis in a cohort of brain cancer patients.

Methods and Materials

MR-CT-compatible head phantom

An MR-CT-compatible 3-dimensional (3D) Anthropomorphic Skull Phantom (CIRS Inc, Norfolk, VA) (Fig. 1A) was first used to evaluate the overall IGRT workflow. The phantom consists of skull and spine bones made of plastic-based tissue substitutes, soft tissues derived from water-based polymers, and a grid inside the cranium (3D matrix of 3-mm diameter rods spaced 1.5 cm apart) to serve as landmarks. The phantom has simulated ear canals (3 mm diameter, 17 mm long) and external markers for localization. Although the phantom cannot provide varying tissue properties like patient data, the 3D-printed skull allowed for benchmarking of the overall IGRT accuracy and could be imaged across several IGRT platforms.

Patient population

Twelve patients (mean age, 60.8 ± 13.3 years) undergoing RT for brain cancer, of whom 1 patient underwent 2 treatment courses, were consented to an institutional review board—

approved prospective protocol for scanning with an investigational ultrashort echo time (UTE)/Dixon MRI sequence. Within 1 week of CT simulation (CT-SIM), all patients underwent an adjunct MR simulation (MR-SIM). Patients were treated (6 ± 9 fractions; range, 1–28) on the Novalis TX, TrueBeam, Trilogy, or Edge linear accelerator platforms (Varian Medical Systems, Palo Alto, CA) according to our standard of care using CT-SIM for treatment planning and IGRT. For 2 patients with >20 fractions, the first 4 fractions were evaluated to avoid disproportionate weighting of the data. All subsequent analysis was performed in an offline retrospective manner.

CT image acquisition

All treatment planning CT images were acquired using a Brilliance Big Bore scanner (Philips Healthcare, Cleveland, OH) with 120 kVp, 284 mAs, 0.814 ± 0.814 mm^2 in-plane spatial resolution, and 1-mm slice thickness. All patients were immobilized using a head frame combined with thermoplastic mask.

MRI acquisition

The MR images were acquired with a 1.0-T Panorama High-Field Open Magnetic Resonance System (Philips Medical Systems, Cleveland, OH) using an 8-channel head coil. Due to the presence of the head coil, the head rest was the only immobilization device that was used during MR-SIM. The UTE/Dixon, T1-FFE, T2-TSE, and fluid attenuation inversion recovery (FLAIR) images were all acquired during MR-SIM for use in our synCT pipeline as described below. UTE/Dixon images were taken with radial acquisition using a triple echo sequence with either TE1/TE2/TE3 = 0.14/3.54/6.94 ms or 0.14/2.44/4.74 ms, TR/α/density of angles = 11.5 ms/25°/75%, and field of view (FOV) = 230–240 mm in all 3 dimensions with 1.2 to 1.3 mm isotropic voxel size. Image parameters for clinical sequences can be found in a previous publication (6).

We have previously characterized the residual gradient nonlinearity distortion (ie, postvendor corrections) at 1.0 T and found them to be <1 mm within 10 cm of isocenter (4). Patient-induced distortions arising from susceptibility and chemical shift have shown a dependence on field strength and can be considered negligible for low field systems (18, 19). In addition, appropriate sequence selection—that is, using turbo spin echo (TSE) sequences and high readout bandwidths (20)—minimized chemical shift and susceptibility-induced distortions. It should be noted that this effect is expected to be small as 99.9% of voxels distorted less than 2.23 ppm for a brain scan acquired at 3T (21), which is equivalent to <1 pixel shift for our acquisition parameters and field strength.

SynCT generation

SynCTs were generated from MR-SIM data sets using a previously described automated image processing pipeline (6). In brief, the automated pipeline consists of 3 major workflows: (*1*) generation of a bone-enhanced image; (*2*) air mask segmentation; and (*3*) final generation of synCTs. Bone-enhanced images are generated by an optimal weighted combination of inverted UTE and water/fat maps automatically generated from the Dixon sequence. The first step of the automated air segmentation was to perform a 3D unwrapping of the phase images using Prelude (22) in FSL (Analysis Group, FMRIB, Oxford, UK) (23,

24), which isolates the susceptibility-induced, chemical shift–related phase, and tissue conductivity–related phase zero maps through solving the set of linear equations common for multiple gradient echo image processing (25, 26). A 6-kernel GMM classifier is then applied to the phase zero map with patient-specific parameters estimated using the expectation maximization algorithm (27). Morphologic filtering and removal of cerebral spinal fluid (CSF) yielded the final air masks. These are inputted into a previously established synCT workflow along with the bone-enhanced, FLAIR, and UTE data sets. Images are automatically segmented using a 5-kernel GMM. A manual assignment process classifies each tissue type as air, bone, fat, brain matter, or CSF. Then, synCTs are generated using a bulk density representation for air, whereas all other tissue types are patient specific with intensities obtained by a voxel-based, weighted summation method from the bone-enhanced, FLAIR, and UTE images described in detail elsewhere (5, 6). Due to the reduced complexity of the phantom, the inverse UTE image and 3-kernel GMM were used for segmentation with slightly different material weightings. Since there was no obvious phase difference in the head phantom, air segmentation was performed manually for the small air volume in the ear canal.

SynCTs were then rigidly registered to the CT image using Elastix (University Medical Center Utrecht, Utrecht, Netherlands) and imported into the Eclipse Treatment Planning System (Eclipse TPS, V11.0, Varian Medical Systems) for further evaluation. SynCTs were validated by calculating the mean absolute error (MAE) between synCT and CT.

DRR generation and evaluation

Once the synCTs were imported into the treatment planning system, setup imaging fields from the clinical treatment plans were copied to the synCTs. For all patients and the skull phantom, DRRs were generated at all cardinal angles using fixed window settings upon export (100–1000 HU). To evaluate the geometric fidelity of the DRRs, a semi-automatic bounding box analysis and landmark evaluation were conducted for the skull phantom. For the bounding box analysis, DRRs were exported to MATLAB (Math-works, Natick, MA) through a DICOM export filter. A manually placed box, with the inferior border set to the bottom of the cranium, was used to isolate the skull from the immobilization devices for analysis. Then, a k-means clustering algorithm with 2 clusters was used to segment the bone, and the resulting image was used to automatically calculate and compare the bounding box width and height. Landmark evaluation was performed by exporting all DRRs through a DICOM filter to ImageJ (available at http://rsb.info.nih.gov/ij) for analysis. A region of interest (ROI) template was generated to plot a line profile through both bone and internal grid landmarks (Fig. 2) at the same location for each DRR, and an automated peak-picking algorithm was used in MATLAB to find the location of local maxima of the landmarks. The peak positions of the landmarks between both DRRs were compared as a surrogate for geometric equivalence.

On-board image acquisition

For the phantom, cone beam CT (CBCT), KV, and MV images were acquired on 3 different linear accelerators (Edge, Novalis TX, TrueBeam) using the clinical presets outlined in Table 1. For the patient study, an offline retrospective evaluation was performed using

available treatment positioning verification data including CBCT, kV/kV, and/or MV/kV planar imaging according to clinical protocol. Table 1 summarizes the acquisition parameters and fractions used for offline registration. Verification images were exported from Eclipse TPS using an integrated DICOM filter (Image Browser, V11.0).

Planar image registrations

Offline retrospective 2D-2D rigid registrations were performed for both planar images/synCT DRRs and planar images/CT DRRs using an in-house developed MATLAB program with rigid registrations performed in Elastix (details in Appendix E1; available online at www.redjournal.org). To assess registration reproducibility, 10 repeat registrations were performed for a subset of 8 fractions for 5 patients (80 registrations). A new ROI was drawn for each registration to include this uncertainty in the reproducibility analysis. Registration quality was determined by visual inspection and normalized mutual information (NMI) metric. Patient shifts were compared for equivalence with the clinical standard (registration between planar images/CT DRRs), and the resulting margins were calculated by the van Herk formalism (28) (95% minimum dose to clinical target volume [CTV] in 90% of patients).

Volumetric (CBCT) image registrations

The 3D rigid registrations were performed between daily CBCT images and synCTs using the Image Registration Workspace in Eclipse. Images were manually registered before adjusting a cubic ROI around the patient skull and performing an automated registration using 3 degrees of freedom, which is consistent with our clinical protocol. Registration reproducibility was evaluated through 10 repeat registrations for a subset of 5 patients. Registration quality was determined by visual inspection, and the results were compared for equivalence to the CBCT/CT registration. Margins were calculated as described for planar image registrations.

Results

SynCT MAE

The full FOV phantom MAE was 63.8 HU (bone MAE = 159.2 HU and soft tissue MAE = 17.3 HU). The patient MAE was 149.2 ± 8.7 HU (range, 138.3–166.2 HU), with tissue MAE of 54.70 ± 21.93 HU and bone MAE of 427.42 ± 38.78 HU.

Geometric evaluation of phantom DRRs

Figure 2 demonstrates the line profile comparison across phantom landmarks between the phantom CT DRRs and synCT DRRs for both right lateral and anterior projections. Overall, consistent geometry was observed between the CT and synCT DRRs. The largest difference in peak location was 1 pixel (0.98 mm) for both the A-P and the R-L comparisons. Bounding box analyses were comparable between CT and synCT yielding 0 and 1 mm height and width differences for A-P DRRs and 1 mm and 0 mm height and width differences, respectively, for R-L DRRs (rounded to nearest pixel). Slight differences in peak intensity values were observed between CT and synCT in the phantom (33% ± 11% peak difference).

Phantom registration results

For the phantom scans, shift differences between registrations with CT-DRRs and registrations with synCT-DRRs using KV images from the Edge were 0.1, −0.1, and −0.1 mm for the L-R, A-P, and S-I axes, respectively. For Novalis TX MV and KV images, the differences were −0.4, −0.1, and −0.1 mm, and for TrueBeam KV images, the differences were −0.2, 0.1, and 0.1 mm for the L-R, A-P, and S-I axes, respectively. The CBCT/CT and CBCT/synCT registrations were <0.4 mm different across all linear accelerators.

Patient results

Planar image registrations—Upon visual inspection, automatic rigid registrations did not require additional manual shifts. Negligible differences in similarity metrics (NMIs) were found between rigid registration results: A-P registration yielded 0.925 ± 0.004 (range, 0.917–0.931) for CT-SIM and 0.926 ± 0.005 (range, 0.919–0.935) for synCT. For lateral projections, NMIs were 0.917 ± 0.009 (range, 0.897–0.933) and 0.913 ± 0.012 (range, 0.885–0.927) for CT-SIM and synCT, respectively. Figure 3 shows the registration translations for the reproducibility analysis. The standard deviations (range, 0.0–0.6 mm) depict the amount of registration variability for each subject. Figure 4 (left) summarizes the distribution of translation differences between registrations performed on patient CT DRRs and synCT DRRs. The largest differences occur in the S-I axis (mean, 0.4 ± 0.5 mm; range, −0.6 to 1.6 mm). Differences in the L-R axis were 0.0 ± 0.5 mm (range, −0.9 to 1.2 mm) and for the A-P axis were 0.1 ± 0.3 mm (range, −0.7 to 0.6 mm). The calculated synCT margins differed by <0.1 mm for both the S-I and the A-P axes and <0.2 mm for the L-R axis as compared with margins derived from CT-SIM reference data sets.

Figure 5 illustrates the DRRs for 2 different patients. Patient 1 yielded typical results for the population, with ~0.1 mm differences in registration for both the 2D/2D and CBCT registrations and with a synCT MAE of 149.5 HU. The registrations for patient 2, by contrast, had the largest discrepancies between CT DRRs and synCT DRRs (~0.8 mm) and synCT MAE of 140.5 HU.

Volumetric image registrations—The reproducibility analysis of volumetric registrations in the patient cohort yielded an average standard deviation of 0.3 (range, 0.1–0.7). Figure 4 (right) summarizes the distribution of shift differences between CBCT registrations performed on patient images for the different reference data sets. The largest differences occurred in the S-I axis (mean, 0.6 ± 0.4 mm; range, −0.2 to 1.6 mm), followed closely by the L-R axis (mean, 0.2 ± 0.4 mm; range, −0.3 to 1.2 mm), and the A-P axis (mean, 0.2 ± 0.3 mm; range, −0.2 to 1.2 mm). The calculated margin differences between synCT and CT-SIM reference data sets were <0.1 mm in the S-I axis and <0.3 mm in both the A-P and L-R axes.

Discussion

The accuracy and reliability of conducting IGRT with synCT data have been compared with the use of CT-SIM. In the phantom, geometric DRR evaluation yielded comparable results between CT and synCT based on landmark analysis. However, slight differences in peak

intensity values were observed in the phantom, whereas these were not as apparent in the patient DRRs (Fig. 5). This is likely a result of the synCT algorithm being optimized for variable tissue contrasts present in patients as compared with the phantom. Intensity discrepancies were observed for patient 2 near the region of the resection cavity as a result of misclassification. Nonetheless, the registration uncertainty for this case was <1 mm between the synCT and CT references. Our results are consistent with a recent comparison between 10 paired points for MR/CT DRRs, yielding a mean difference of −0.05 ± 0.85 mm (maximum of ~2 mm) (29). Our bounding box analysis for the phantom also demonstrated differences between the overall skull geometries within this range. A limitation of using the head phantom for synCT validation is that some components (ie, air-filled ear canals and nearby material) did not yield a detectable MR signal (Fig. 1H). This resulted in an inaccurate segmentation of the air cavity with some material misclassified as bone. Nevertheless, the landmarks were sufficient for analyzing the geometric integrity of synCT DRRs.

The largest patient MAE deviations were observed near the segmented bone and air regions, where the impact of misregistration and segmentation errors will contribute to higher MAEs. The overall MAE is consistent with the range reported in our previous feasibility study developing the synCT pipeline using fewer patients (147.5 ± 8.3 HU) (6) as well as in the literature (8, 10). The registration reproducibility analysis showed that the magnitude of variability was patient dependent. Two patients with the highest standard deviations in the S-I direction were each found to have a partially distorted cerebrum after resection (Fig. 3, patients 2 and 5). However, the largest standard deviations were 0.6 mm for 2D/2D and 0.7 mm for volumetric registrations. These values are within the expected variability for automated planar (30) and volumetric CBCT registrations (31) for IGRT systems (32).

On average, patient registration differences were largest in the S-I axes (0.2 mm larger on average). A possible explanation could be related to the slightly larger CT slice thickness (~1 mm) as compared with the in-plane resolution (0.8 mm). For both 2D/2D and volumetric registrations, the margins calculated for synCT were within 0.3 mm of those calculated for CT for all axes. Patient 2 had a large piece of the skull surgically removed (Fig. 5); thus, intensity differences were present between the CT and synCT generated DRRs in the resected area and adversely affected the synCT DRR quality. Even though these evaluations included residual uncertainty of the registrations, in this worst-case scenario, the overall registration differences between CT and synCT were still within the reported registration error for IGRT systems (0.4–1.1 mm) (30–32).

Yin et al (33) showed that MR-DRRs and CT-DRRs were within 2.5 mm in a phantom and patient case using chamfer matching, although the MRI acquisition was not optimized for MR simulation (ie, 5-mm slice thickness, 2.5-mm slice spacing). Using thinner slice thicknesses is a key component to generating accurate DRRs. During our initial synCT brain algorithm development, we highlighted 2 of 10 cases that required modified air masks in the frontal sinus region through an additional postprocessing step using the UTE magnitude image and morphologic erosion (4). This modification increased the true positive rate (TPR) agreement with CT-SIM air segmentation by 2% and 5% for the 2 patients. However, applying this technique for the rest of the cohort did not change their TPR results (<0.1%

difference). In the current IGRT evaluation, rigid registrations were performed using the entire cranium. In partial brain settings, portions of the brain could be used during registration that may influence registration performance. If a localized portion near the frontal sinus, where uncertainty may be greater, were used, caution would need to be exercised to ensure accurate synCT geometry. The performance of synCT DRRs for IGRT using partial brain information for localization will be explored in future work. Recently, oblique ExacTrac brain images were registered to UTE-based synCTs in 7 patients, and the registrations were <1 mm/1° different (12). Our results were consistent with this work and with another study by Edmund et al (17) (<1 mm difference).

To translate to other field strengths, UTE-Dixon acquisition parameters would need to be optimized, and postprocessing corrections for bias field and patient-specific distortions would be required. Putting our findings into clinical context, the recommended CTV-to-PTV margins for IMRT range from 3 to 5 mm for glioblastomas (34); thus, our registration errors using synCTs as the reference data set were within a clinically acceptable range (ie, <0.3 mm difference in margin calculation). Previously, we found that the synCT plan quality met all clinical criteria with no systematic differences when used as the primary treatment planning data set (14). These data, when taken in concert with the IGRT study, suggest that MR-only treatment planning is feasible for selected patients receiving partial brain RT. One recent study suggests that the level of MR-only accuracy in the brain is sufficient for stereotactic applications (12). Several groups have conducted end-to-end testing of an MR-only work-flow (35, 36), and clinical studies are currently under way.

Conclusions

Using a previously developed synCT methodology, we have quantified the accuracy of using synCT in an IGRT pipeline relative to the clinical standard, CT, in the brain. For typical cases, the characterized differences between the use of synCT and CT were within the expected errors associated with image registration. A prospective clinical trial is warranted to determine the potential gains of MR-only treatment planning.

Supplementary Material

Refer to Web version on PubMed Central for supplementary material.

References

1. van Herk M, Kooy HM. Automatic three-dimensional correlation of CT-CT, CT-MRI, and CT-SPECT using chamfer matching. Med Phys. 1994; 21:1163–1178. [PubMed: 7968850]
2. Ulin K, Urie MM, Cherlow JM. Results of a multi-institutional benchmark test for cranial CT/MR image registration. Int J Radiat Oncol Biol Phys. 2010; 77:1584–1589. [PubMed: 20381270]
3. Baldwin LN, Wachowicz K, Thomas SD, et al. Characterization, prediction, and correction of geometric distortion in 3 T MR images. Med Phys. 2007; 34:388–399. [PubMed: 17388155]
4. Price RG, Kadbi M, Kim J, Balter J, Chetty IJ, Glide-Hurst CK. Technical note: Characterization and correction of gradient nonlinearity induced distortion on a 1. 0 T open bore MR-SIM. Med Phys. 2015; 42:5955. [PubMed: 26429270]
5. Kim J, Glide-Hurst C, Doemer A, Wen N, Movsas B, Chetty IJ. Implementation of a novel algorithm for generating synthetic CT images from magnetic resonance imaging data sets for

prostate cancer radiation therapy. Int J Radiat Oncol Biol Phys. 2015; 91:39–47. [PubMed: 25442341]

6. Zheng W, Kim JP, Kadbi M, Movsas B, Chetty IJ, Glide-Hurst CK. Magnetic resonance-based automatic air segmentation for generation of synthetic computed tomography scans in the head region. Int J Radiat Oncol Biol Phys. 2015; 93:497–506. [PubMed: 26460991]
7. Hsu SH, Cao Y, Huang K, et al. Investigation of a method for generating synthetic CT models from MRI scans of the head and neck for radiation therapy. Phys Med Biol. 2013; 58:8419–8435. [PubMed: 24217183]
8. Johansson A, Karlsson M, Nyholm T. CT substitute derived from MRI sequences with ultrashort echo time. Med Phys. 2011; 38:2708–2714. [PubMed: 21776807]
9. Andreasen D, Van Leemput K, Hansen RH, et al. Patch-based generation of a pseudo CT from conventional MRI sequences for MRI-only radiotherapy of the brain. Med Phys. 2015; 42:1596–1605. [PubMed: 25832050]
10. Sjolund J, Forsberg D, Andersson M, et al. Generating patient specific pseudo-CT of the head from MR using atlas-based regression. Phys Med Biol. 2015; 60:825–839. [PubMed: 25565133]
11. Korhonen J, Kapanen M, Keyrilainen J, et al. A dual model HU conversion from MRI intensity values within and outside of bone segment for MRI-based radiotherapy treatment planning of prostate cancer. Med Phys. 2014; 41:011704. [PubMed: 24387496]
12. Yang Y, Cao M, Kaprealian T, et al. Accuracy of UTE-MRI-based patient setup for brain cancer radiation therapy. Med Phys. 2016; 43:262–267. [PubMed: 26745919]
13. Paradis E, Cao Y, Lawrence TS, et al. Assessing the dosimetric accuracy of magnetic resonance-generated synthetic CT images for focal brain VMAT radiation therapy. Int J Radiat Oncol Biol Phys. 2015; 93:1154–1161. [PubMed: 26581151]
14. Kim J, Garbarino K, Schultz L, et al. Dosimetric evaluation of synthetic CT relative to bulk density assignment-based magnetic resonance-only approaches for prostate radiotherapy. Radiat Oncol. 2015; 10:239. [PubMed: 26597251]
15. Uh J, Merchant TE, Li Y, et al. MRI-based treatment planning with pseudo CT generated through atlas registration. Med Phys. 2014; 41:051711. [PubMed: 24784377]
16. Korhonen J, Kapanen M, Sonke JJ, et al. Feasibility of MRI-based reference images for image-guided radiotherapy of the pelvis with either cone-beam computed tomography or planar localization images. Acta Oncol. 2015; 54:889–895. [PubMed: 25233439]
17. Edmund JM, Andreasen D, Mahmood F, et al. Cone beam computed tomography guided treatment delivery and planning verification for magnetic resonance imaging only radiotherapy of the brain. Acta Oncol. 2015; 54:1496–1500. [PubMed: 26198652]
18. Stanescu T, Wachowicz K, Jaffray DA. Characterization of tissue magnetic susceptibility-induced distortions for MRIGRT. Med Phys. 2012; 39:7185–7193. [PubMed: 23231269]
19. Baldwin LN, Wachowicz K, Fallone BG. A two-step scheme for distortion rectification of magnetic resonance images. Med Phys. 2009; 36:3917–3926. [PubMed: 19810464]
20. Paulson ES, Erickson B, Schultz C, et al. Comprehensive MRI simulation methodology using a dedicated MRI scanner in radiation oncology for external beam radiation treatment planning. Med Phys. 2015; 42:28. [PubMed: 25563245]
21. Wang H, Balter J, Cao Y. Patient-induced susceptibility effect on geometric distortion of clinical brain MRI for radiation treatment planning on a 3T scanner. Phys Med Biol. 2013; 58:465–477. [PubMed: 23302471]
22. Jenkinson M. A fast, automated, N-dimensional phase unwrapping algorithm. Magn Reson Med. 2003; 49:193–197. [PubMed: 12509838]
23. Smith SM, Jenkinson M, Woolrich MW, et al. Advances in functional and structural MR image analysis and implementation as FSL. Neuroimage. 2004; 23:S208–S219. [PubMed: 15501092]
24. Woolrich MW, Jbabdi S, Patenaude B, et al. Bayesian analysis of neuroimaging data in FSL. Neuroimage. 2009; 45:S173–S186. [PubMed: 19059349]
25. Hines CD, Yu H, Shimakawa A, et al. T1 independent, T2* corrected MRI with accurate spectral modeling for quantification of fat: Validation in a fat-water-SPIO phantom. J Magn Reson Imaging. 2009; 30:1215–1222. [PubMed: 19856457]

26. Kim DH, Choi N, Gho SM, et al. Simultaneous imaging of in vivo conductivity and susceptibility. Magn Reson Med. 2014; 71:1144–1150. [PubMed: 23606054]
27. Dempster AP, Laird NM, Rubin DB. Maximum likelihood from incomplete data via the EM algorithm. J R Stat Soc Series B Stat Methodol. 1977; 39:1–38.
28. van Herk M, Remeijer P, Lebesque JV. Inclusion of geometric uncertainties in treatment plan evaluation. Int J Radiat Oncol Biol Phys. 2002; 52:1407–1422. [PubMed: 11955756]
29. Yu H, Caldwell C, Balogh J, et al. Toward magnetic resonance-only simulation: Segmentation of bone in MR for radiation therapy verification of the head. Int J Radiat Oncol Biol Phys. 2014; 89:649–657. [PubMed: 24803040]
30. Fox T, Huntzinger C, Johnstone P, et al. Performance evaluation of an automated image registration algorithm using an integrated kilo-voltage imaging and guidance system. J Appl Clin Med Phys. 2006; 7:97–104. [PubMed: 16518321]
31. Arumugam S, Jameson MG, Xing A, et al. An accuracy assessment of different rigid body image registration methods and robotic couch positional corrections using a novel phantom. Med Phys. 2013; 40:031701. [PubMed: 23464296]
32. Sharma SD, Dongre P, Mhatre V, et al. Evaluation of automated image registration algorithm for image-guided radiotherapy (IGRT). Australas Phys Eng Sci Med. 2012; 35:311–319. [PubMed: 22948720]
33. Yin F-F, Gao Q, Xie H, et al. MR image-guided portal verification for brain treatment field. Int J Radiat Oncol Biol Phys. 1998; 40:703–711. [PubMed: 9486623]
34. Radiation Therapy Oncology Group. [Accessed April 5, 2016] RTOG 0825: Phase III double-blind placebo-controlled trial of conventional concurrent chemo-radiation and adjuvant temozolomide plus bevacizumab versus conventional concurrent chemoradiation and adjuvant temozolomide in patients with newly diagnosed glioblastoma. Available at: https://www.rtog.org/ClinicalTrials/ProtocolTable/StudyDetails.aspx?study=0825
35. Korsholm ME, Waring LW, Edmund JM. A criterion for the reliable use of MRI-only radiotherapy. Radiat Oncol. 2014; 9:16. [PubMed: 24405515]
36. Sun J, Dowling J, Pichler P, et al. MRI simulation: End-to-end testing for prostate radiation therapy using geometric pelvic MRI phantoms. Phys Med Biol. 2015; 60:3097–3109. [PubMed: 25803177]

Summary

The accuracy and reliability of applying synthetic computed tomography (CT) (synCT) derived from magnetic resonance imaging (MRI) for image guided radiation therapy have been quantitatively characterized relative to the clinical standard, CT. Phantom data revealed that the geometric accuracy of digitally reconstructed radiographs generated from synCT were comparable with CT. In a patient cohort, volumetric and planar registrations performed with synCT were within clinically acceptable tolerances, with negligible changes in margin calculation. This work supports the implementation of MRI-only treatment planning for the brain.

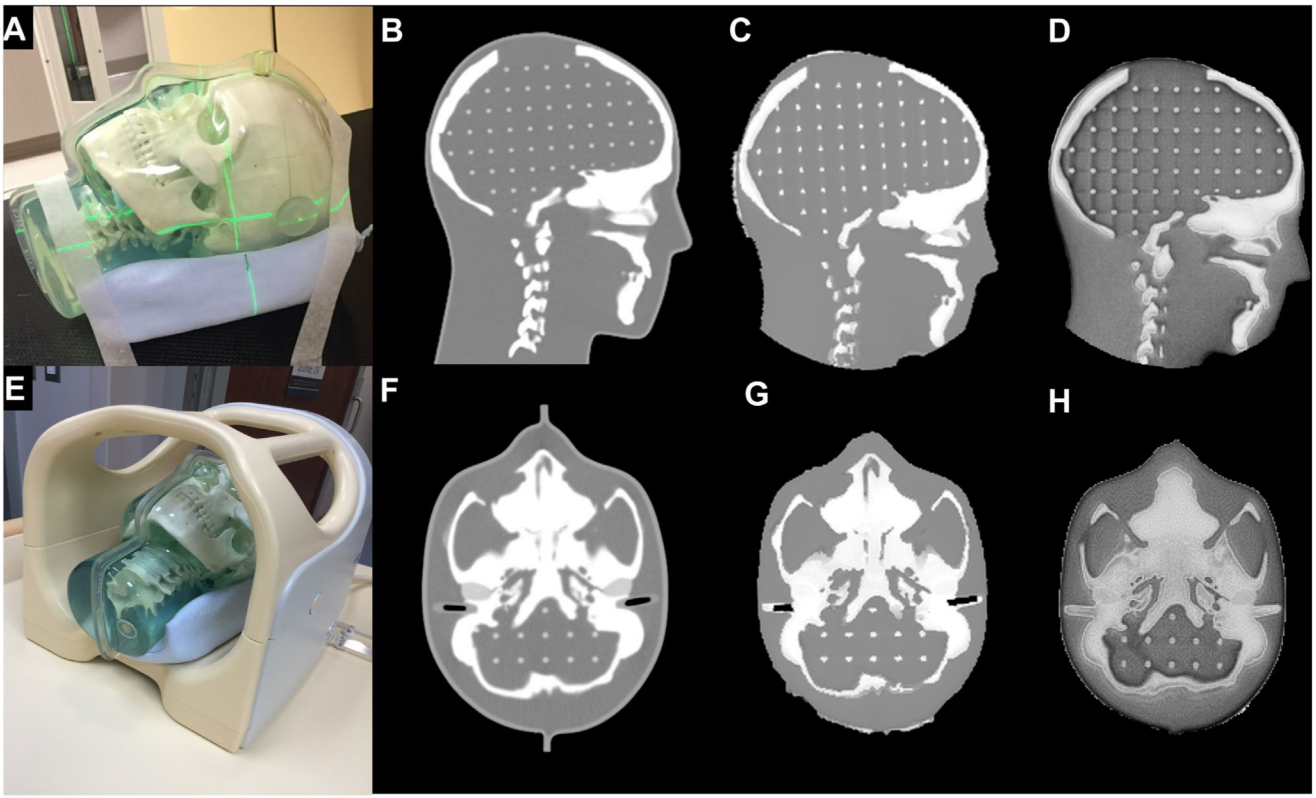

Fig. 1.

(A) Magnetic resonance–computed tomography (MR-CT)-compatible phantom on CT simulation (CT-SIM) table. (B) Sagittal CT. (C) Sagittal synCT. (D) Sagittal MRI (inverted ultrashort echo time [UTE]). (E) Phantom in 8-channel head coil on MR simulation (MR-SIM) table. (F) Axial CT. (G) Axial synCT. (H) Axial MRI (inverted UTE).

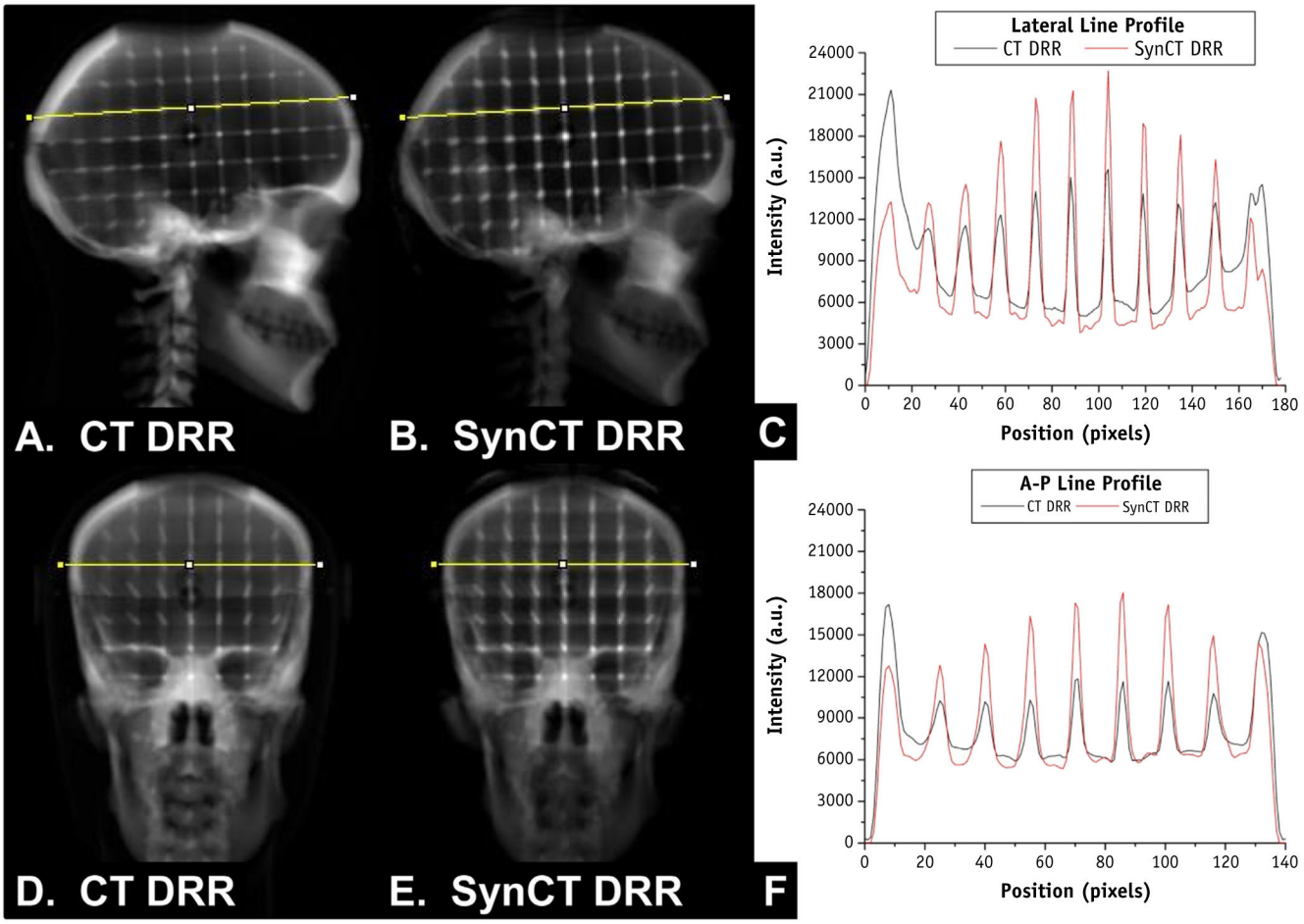

Fig. 2.

(A) Phantom lateral digitally reconstructed radiograph (DRR) generated from computed tomography (CT). (B) Phantom lateral DRR generated from synthetic CT (synCT). (C) Image intensity profiles across the line profile for the lateral CT and synCT DRRs shown in (A) and (B). (D) Anterior-posterior (A-P)-DRR generated from CT. (E) A-P-DRR generated from synCT. (F) Image intensity profiles across line profiles shown in (D) and (E) for A-P CT-DRR and synCT-DRR. Profile analysis was used for landmark evaluation to assess the synCT geometric integrity.

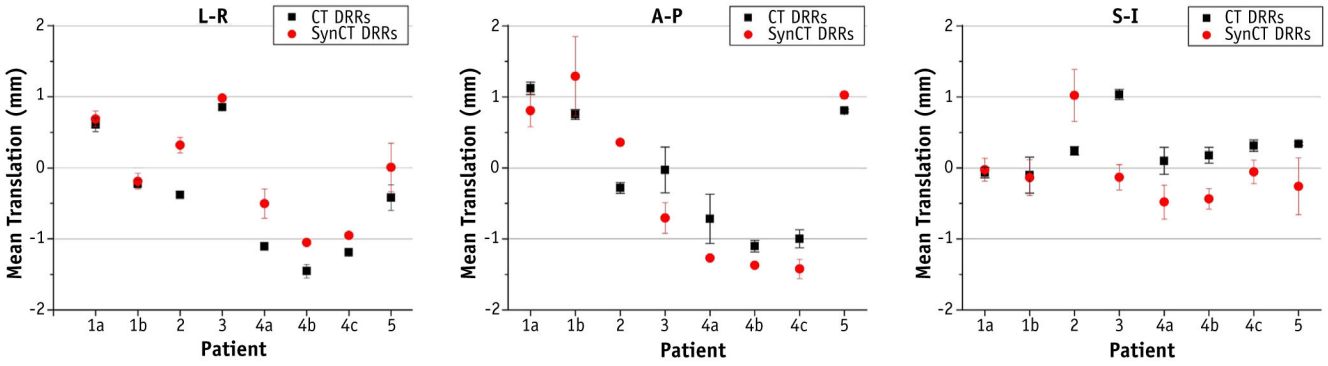

Fig. 3.

Planar image registration reproducibility assessment of an in-house image registration program for 5 different patients (8 fractions) using 10 repeated registrations. Mean and standard deviation of the registration translations are shown for each series. *Abbreviations:* A-P = anterior-posterior; L-R = left-right; S-I = superior-inferior.

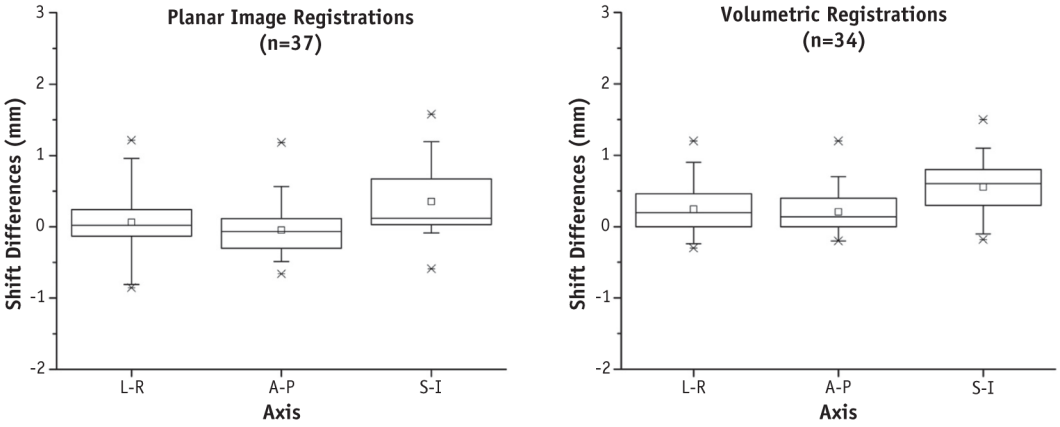

Fig. 4.

Distribution of registration differences obtained when synthetic computed tomography (synCT) and CT data were used for reference data sets for the patient cohort. Left, planar image registration differences. Right, volumetric registration shift differences. Boxplots, dotted line, and circle indicate interquartile range, mean, and median, respectively. Whiskers indicate fifth and 95th percentile, x's mark first and 99th percentile, and dashes mark the minimum and maximum shift differences. *Abbreviations:* A-P = anterior-posterior; L-R = left-right; S-I = superior-inferior.

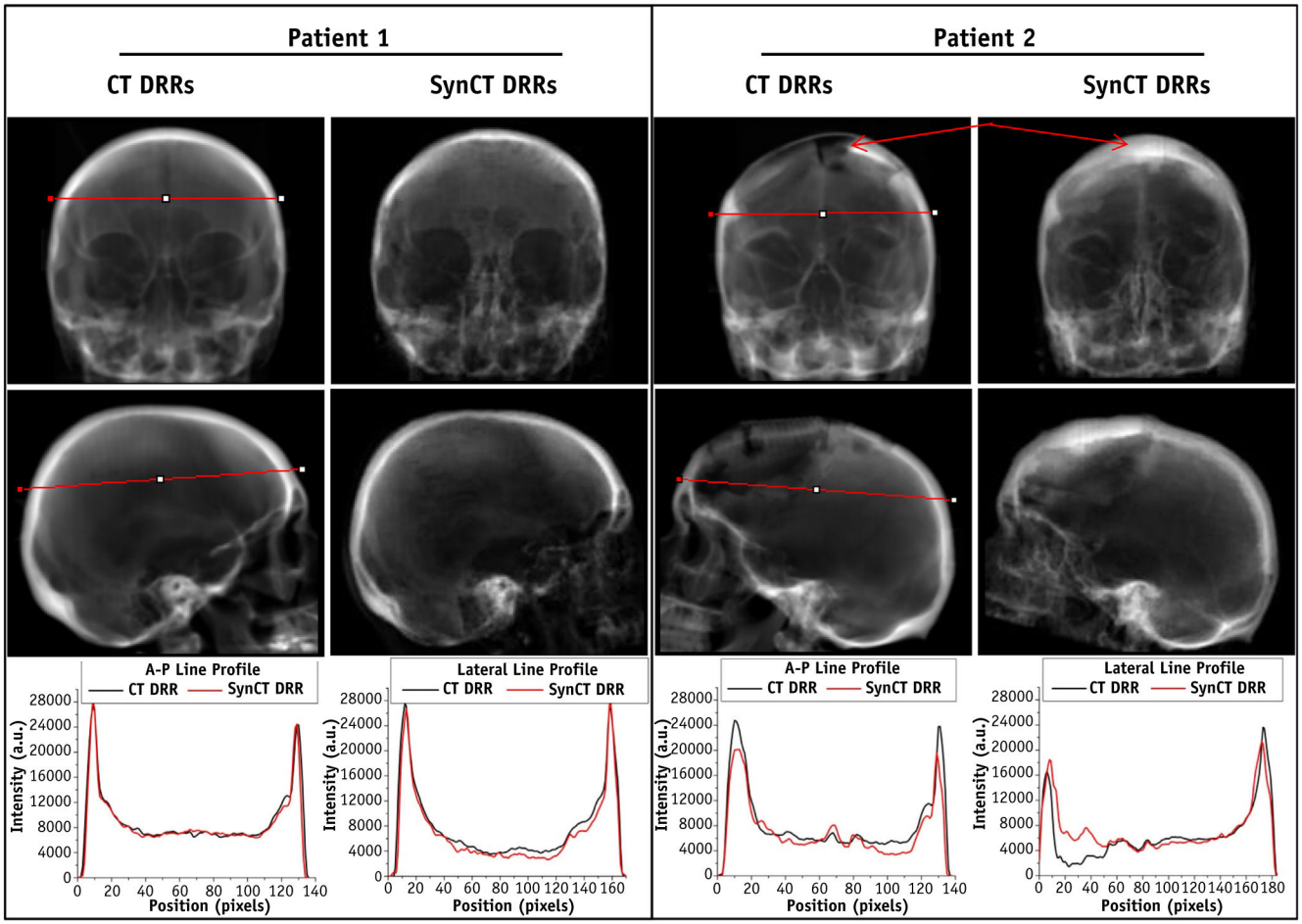

Fig. 5.

Anterior-posterior (A-P) (top row) and lateral (middle row) computed tomography digitally reconstructed radiographs (CT-DRRs) and synthetic computed tomography digitally reconstructed radiographs (synCT-DRRs) with respective intensity line profiles for patients 1 and 2. Patient 1 represents typical results for the population. Patient 2 yielded the largest discrepancies in registration (~0.8 mm) because of the impact of resection on DRR quality (arrows).

Table 1

On-board image acquisition parameters and distribution of fractions treated for the 4 linear accelerator platforms

Linear accelerator platform	CBCT					AP planar imaging				Lateral planar imaging			
	kVp	mAs	In-plane resolution (mm^2)	ST (mm)	Fx	kVp	mAs	Resolution (mm^2)	Fx	kVp	mAs	Resolution (mm^2)	Fx
TrueBeam	100	147	0.511 × 0.511	1	4	85	5	0.259 × 0.259	7	70	5	0.259 × 0.259	7
Trilogy	100	148	0.488 × 0.488	3	5	100	8	0.259 × 0.259	4	70	5	0.259 × 0.259	4
Edge	100	147–267	0.511 × 0.511 to 0.513 × 0.513	1	16	85	8	0.259 × 0.259	23	70	5	0.259 × 0.259	23
Novalis Tx	80–100	738–740	0.488 × 0.488 to 0.511 × 0.511	1	9	6 MV	N/A	0.261 × 0.261	3	70	5	0.259 × 0.259	3
Total images analyzed					34	Total images analyzed			37	Total images analyzed			37

Abbreviations: AP = anterior-posterior; CBCT = cone beam computed tomography; Fx = fraction; N/A = not applicable; ST = slice thickness.